

1 **Accommodative holography: improving accommodation response for**
2 **perceptually realistic holographic displays - Supplementary Material**

3
4 DONGYEON KIM* and SEUNG-WOO NAM*, Seoul National University, Republic of Korea

5 BYOUNGHYO LEE, Seoul National University, Republic of Korea

6 JONG-MO SEO, Seoul National University, Republic of Korea

7 BYOUNGHO LEE, Seoul National University, Republic of Korea

8
9 **ACM Reference Format:**

10
11 Dongyeon Kim, Seung-Woo Nam, Byoungkyo Lee, Jong-Mo Seo, and Byoungho Lee. 2022. Accommodative holography: improving
12 accommodation response for perceptually realistic holographic displays - Supplementary Material. *ACM Trans. Graph.* 41, 4, Article 111
13 (July 2022), 12 pages. <https://doi.org/10.1145/3528223.3530147>

14
15 **S1 ADDITIONAL DETAILS ON IMPLEMENTATION**

16
17 **System**

18
19 Figure S1 shows an overview of the benchtop prototype utilized in the experimental evaluations. The fiber-coupled laser
20 diode (LD, WikiOptics) emanates a full-color beam with the wavelength of 638 nm, 520 nm, and 450 nm. A consecutive
21 placement of an objective lens (OL) with a numerical aperture of 0.25 (Newport, M-10X) and a collimating lens (CL)
22 with a focal length of 100 mm (Zeiss, Milvus 100 mm, f/2) collimates the laser beam with high uniformity. As mentioned
23 in Section 5.1, a FLCoS SLM and an LCoS SLM provided with the corresponding CGHs are optically relayed with a
24 series of lenses, respectively. In the optical arm of FLCoS SLM, the relay optics, which consist of L1 (Nikon, 135mm,
25 f/2.8) and L2 (Nikon, AF-S VR MICRO NIKKOR 105mm, f/2.8), effectively modifies the pixel pitch of FLCoS SLM (Fourth
26 Dimensional Displays, a resolution of 1920 × 1200, a pixel pitch of 8.2 μ m) to 6.4 μ m in the relayed field. A physical
27 filter (F1) that blocks high-order signals and eventually determines the eye-box of the near-eye display is designed as a
28 rectangle with a size of 7.4 mm × 3.7 mm and modeled with a 3D printer is placed at the Fourier plane. On the contrary,
29 the LCoS SLM is relayed with lenses (L3, L4) of an identical model (Nikon, AF-S VR MICRO NIKKOR 105 mm, f/2.8) and
30 the filter (F2) with a size of 7.4 mm × 3.7 mm. The OLED panel of BOE (0.39 inch, resolution of 1920 × 1080) is 1.5 times
31 expanded to match the window size with two different achromatic doublets (L5: Thorlabs, AC508-100-A, L6: Thorlabs,
32 AC508-150-A) and the size of the filter (F3) is determined as 10.5 mm × 5.3 mm to match the effective size of eye-box
33 with the holographic displays.

34
35 The beams merged with multiple beamsplitters (BS) are again relayed with a 4-f system constructed with two
36 identical achromatic doublets (L7, L8: Thorlabs, AC508-150-A). At the Fourier plane, a focus-tunable lens (FTL, Optotune

37
38 *Both authors contributed equally to this research.

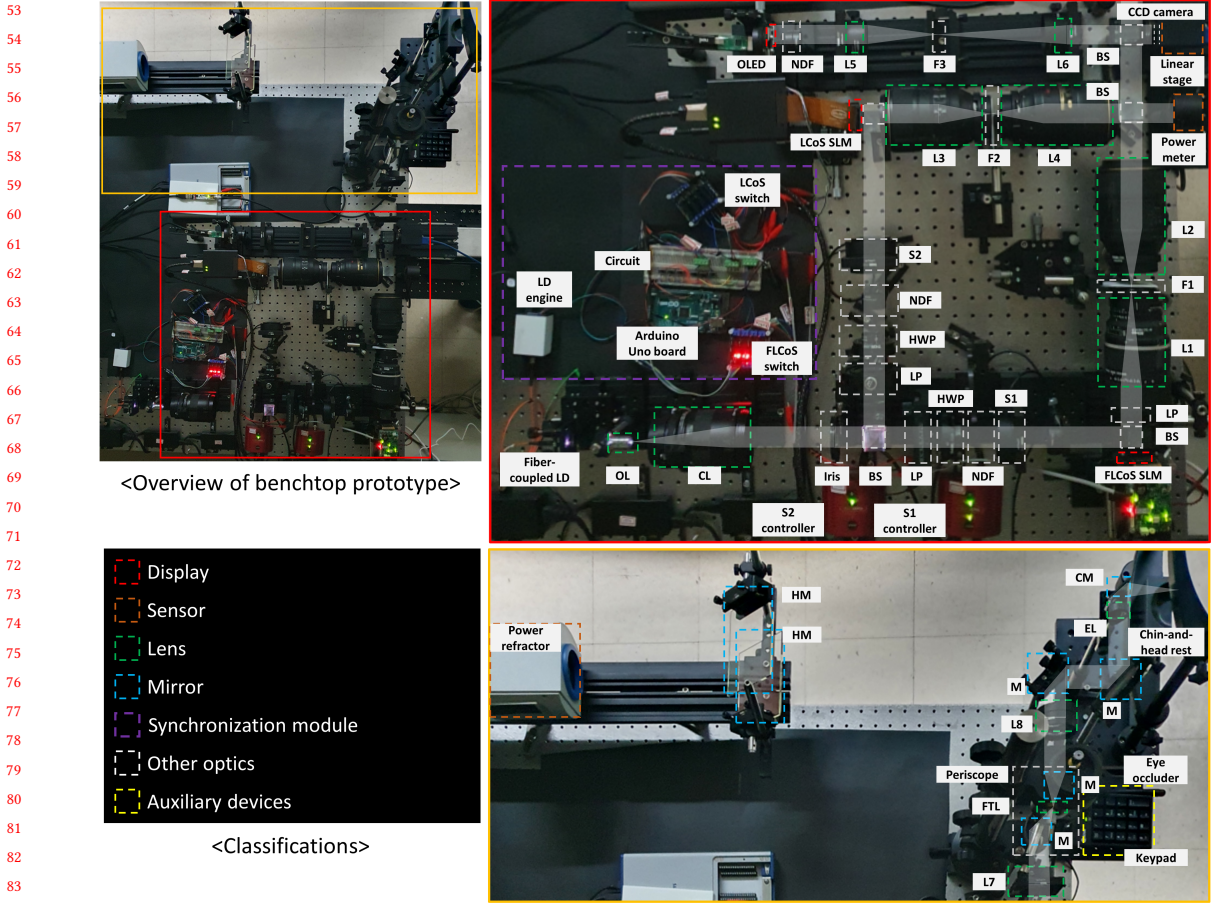
39
40 Authors' addresses: Dongyeon Kim; Seung-Woo Nam, Seoul National University, Republic of Korea; Byoungkyo Lee, Seoul National University, Republic
41 of Korea; Jong-Mo Seo, Seoul National University, Republic of Korea; Byoungho Lee, Seoul National University, Republic of Korea.

42
43 Permission to make digital or hard copies of all or part of this work for personal or classroom use is granted without fee provided that copies are not
44 made or distributed for profit or commercial advantage and that copies bear this notice and the full citation on the first page. Copyrights for components
45 of this work owned by others than ACM must be honored. Abstracting with credit is permitted. To copy otherwise, or republish, to post on servers or to
46 redistribute to lists, requires prior specific permission and/or a fee. Request permissions from permissions@acm.org.

47
48 © 2022 Association for Computing Machinery.

49
50 Manuscript submitted to ACM

51
52 Manuscript submitted to ACM



85 Fig. S1. Overview of the benchtop prototype utilized in the experimental evaluations, the enlarged views of each section (red, orange)
86 with the labeled components, and the inset that describes the classifications of individual components. In the enlarged photographs,
87 the beam paths are colored white to show how the individual displays are visualized. The dashed lines in red, brown, green, blue,
88 purple, and white respectively represent the display device, sensor, lens, mirror, synchronization module, and the other optics to
89 construct the whole system. The auxiliary devices used in the user experiments, such as an eye occluder and a keypad, are highlighted
90 with a yellow dashed line. For the lenses (L), filters (F), and shutters (S), additional indices are provided for convenient reference.

91
92
93 EL-16-40-TC-VIS-5D-C) is placed to change the axial depth of the reconstructed image and controlled with the calibrated
94 analog signal generated by a data acquisition board (National Instrument, USB-6343). The FTL is placed parallel to the
95 ground to alleviate the aberration due to a gravitational force. The height of the whole display system is adjusted to an
96 eye-level by putting a periscope (Newport) equipped with two flat mirrors. After beams are deflected with two mirrors,
97 a 1-inch eyepiece lens (EL, Thorlabs, AC254-075-A) with a focal length of 75 mm is placed to virtually floating the
98 image. The overall eye-box of the near-eye display system is provided as 5.27 mm × 2.64 mm, and the field of view is
99 7.8° × 4.4°.
100

101 For the accommodation experiments, the power refractor of Plusoptix (PowerRef3) measures an eye's refractive
102 power with a speed of 50 Hz. The projection distance is given as 1.0 m from the eye, and a series of hot mirrors (Edmund
103 Manuscript submitted to ACM

105 optics, #64-472) and a cold mirror (Edmund optics, #64-449) is placed for robust capture of one's retina with infrared
106 light. For full-color holographic displays, the TTL signals generated by each SLM are actively switched with two electric
107 switches (LCoS switch, FLCoS switch) attached to the main circuit to provide a single TTL signal to the LD engine.
108 Here, the shutters (S1, S2) and the connected controllers are also synchronized with the corresponding switches for
109 automated pairwise comparisons with a single LD source. The entire system is managed with an Arduino Uno board.
110 The images are captured with a charge-coupled device (CCD) (FLIR, GS3-U3-91S6C) having a resolution of 3376×2704
111 and a pitch of $3.69 \mu\text{m}$ at the IP. The dioptric distance of 0.6 D is converted to 2.8 mm, and the CCD is translated with
112 the help of the motorized linear stage (Newport, FCL100). We additionally equipped an eye occluder to block the other
113 eye during accommodation experiments, and a keypad to enter user response in preference experiments.
114
115
116

117 **Apparatus**

118 The optical powers of the individual holographic scenes are measured with the optical power detector (Newport,
119 918D-SL-OD3R) with a circular aperture of 11.3 mm connected to the power meter (Newport, 2936-R) as shown in Fig.
120 S1. The light fluxes of two holographic displays are balanced by placing NDFs with different transmittance ratios. The
121 averaged optical powers of the reconstructed scenes (lion, market, castle, and castle with a Maltese cross) in red (638
122 nm), green (520 nm), blue (450 nm) channel are measured as 1.6 nW, 1.8 nW, and 2.5 nW, respectively. The converted
123 luminance is estimated as 0.2 cd/m^2 , which is far below the permissible level of laser exposure.
124
125
126

127 **Off-axis holographic displays**

128 It is well known that the undiffracted lights are inherently present in on-axis holographic displays due to the finite fill
129 factor of SLMs. For example, the phase-only SLM (Holoeye, LETO-3 CFS-127) used in our experiments has a fill factor
130 of 93 %. The undiffracted light can be harmful to the user's eye when directly viewing the holographic display and can
131 hardly be managed in an on-axis configuration. Thus, we vertically rotated both SLMs in half of the diffraction angle
132 of the blue signal to eliminate the potential risk. Accordingly, the bandwidths of CGHs are also vertically-halved and
133 shifted to reconstruct the off-axis holographic image.
134
135
136

137 **Automated pairwise comparisons**

138 The holograms were provided by Holoeye's built-in SDK for LCoS SLM and OpenGL codes for FLCoS SLM. For FLCoS
139 SLM, the binary holograms are encoded to 24bit images where a single bit can contain a single binary hologram.
140 The encoded holograms are loaded on the graphics processing unit (GPU) with OpenGL for fast update of CGHs
141 with a maximum frequency of 150 Hz. When an image is reconstructed with a single SLM, the optical path of the
142 counterpart SLM is blocked by the optical shutter placed at the beam path, and these shutters are electrically controlled
143 by the Arduino Uno board. Similarly, the electrical switches are utilized to provide the illumination sequences of the
144 corresponding SLM depending on the trigger provided by the Arduino Uno board as the transistor-transistor logic
145 (TTL) signals of two SLMs are in different forms.
146
147

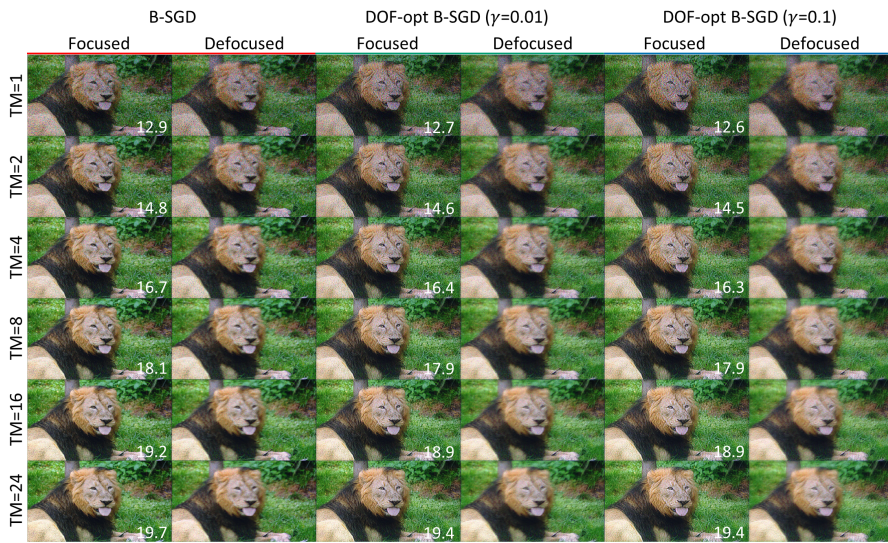
148 The pairwise comparison experiments were performed in a fully-automated manner. The entire experiments were
149 performed with a subject-dependent pre-defined csv file that contains a sequence of options and the user's answers
150 were saved in the corresponding file. Subjects were instructed to enter a response after a beep sound indicating that
151 both options were displayed. If an input other than the desired ones was given, another beep was played to re-enter the
152 response.
153
154

157 **S2 ADDITIONAL EXPERIMENTAL RESULTS**

158

159 **Captured results**

160 Other than the photographs of holographic images shown as Fig. 6, we additionally provide the captured results (focused,
 161 defocused) of three different CGH algorithms (B-SGD, DOF-opt B-SGD ($\gamma = 0.01$), DOF-opt B-SGD ($\gamma = 0.1$)) with six
 162 different temporal multiplexing conditions (TM=1, 2, 4, 8, 16, 24) as Fig. S2-S4. They are provided with three different
 163 images (lion, market, and castle) employed in the subjective image quality evaluations. In the bottom right corner of
 164 the focused images, the measured PSNR values are provided. As the regularization coefficient increases, the measured
 165 PSNR decreases, and the edges of the individual images get enhanced.
 166



188 Fig. S2. Captured results of lion scene utilized in the subjective image quality evaluation. Image sources from DIV2K dataset
 189 [Agustsson and Timofte, 2017].
 190

191 **Tolerance of CGHs on the artifacts**

192

193 In the user experiments performed to evaluate the subjective image quality, some participants reported that the moving
 194 artifacts are present in 8bit-SGD images, although we provided the images as shown in Fig. 6. The noticeable artifact led
 195 to relatively low JOD with large deviations across the subjects. We speculate the artifact roots from the dirt or debris
 196 inherently present in the optical system. Thus, we additionally placed a slide glass with small dirt on it in either the
 197 pupil plane or the image plane of the holographic displays to simulate this phenomenon. Then, we captured results at
 198 the image plane with the CCD camera as shown in Fig. S5.
 199

200 As shown in Fig. S5, the holographic images of B-SGD and 8bit-GS showed the robustness to the artifacts that can be
 201 present in the optical system. However, the 8bit-SGD images showed little tolerance to the artifacts, and the defects with
 202 small ringing patterns get noticeable in the smooth sections of individual images. The images were highly susceptible to
 203 the minute movement of the slide glass as shown in 8bit-SGD with dust#1 at pupil and 8bit-SGD with dust#2 at pupil. If
 204 the artifacts are present in the pupil plane, the defects contain color fringes, easily noticeable in the actual experiments.
 205

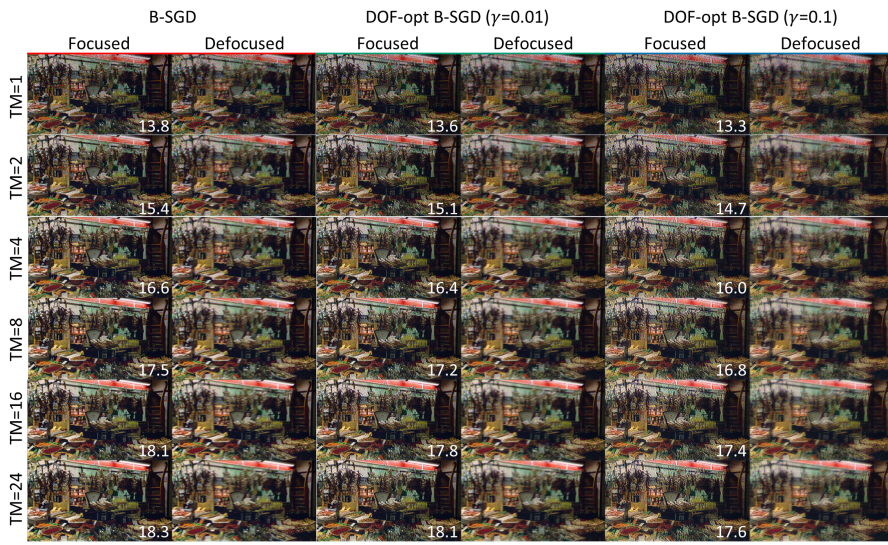


Fig. S3. Captured results of market scene utilized in the subjective image quality evaluation. Image sources from DIV2K dataset [Agustsson and Timofte, 2017].

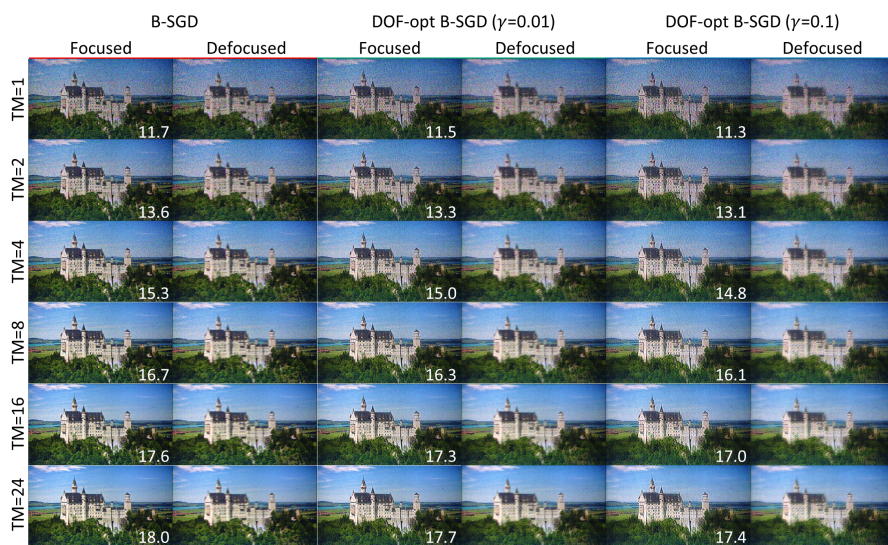


Fig. S4. Captured results of castle scene utilized in the subjective image quality evaluation. Image sources from DIV2K dataset [Agustsson and Timofte, 2017].

This issue can be handled with the recently introduced camera-in-the-loop calibration method [Chakravarthula et al., 2020, Peng et al., 2020] pre-compensating the artifacts with captured images only when the artifact is present in the display optics. The human eye consists of liquid layers and the tear film, which is the very outer part of the eye, is a complex mixture of lipids of different classes [Bron et al., 2004] that may result in undesirable diffraction

Captured results of focused images



Fig. S5. Captured results of holographic images acquired with various CGH algorithms to test the tolerance on the artifacts. Image sources from DIV2K dataset [Agustsson and Timofte, 2017].

and interference. Moreover, human eyes always move even when they are fixated. This raises the question that CGHs reproducing a coherent field with a narrow angular spectrum may not be suitable for practical use in holographic displays, although they demonstrate a superior quality with a single frame in the camera-captured results.

Manuscript submitted to ACM

313 Results of accommodation experiments

314
315 The accommodation responses when viewing the holographic near-eye display prototype providing various CGHs are
316 measured, and the additional results are presented as Fig. S6. Fig. S6(A) demonstrates the normalized accommodative
317 gains averaged across the 21 subjects. They are provided depending on the number of TM frames as speckle reduction
318 showed a strong correlation to the accommodative gain. Finally, we demonstrate the measured accommodation of
319 individual subjects, including the dioptric amplitude estimated when viewing OLED as Fig. S6(B).
320

321 Change in pupil size

322 During the accommodation experiments, we also measured the pupil diameter of users. Figure S7 demonstrates the
323 pupil diameter measured when the subjects view the visual stimulus provided by OLED. We provide pupil diameter
324 change for six cycles of 6 subjects who achieved the highest gains in the experiments. Some subjects showed consistency
325 in the measured pupil size, while others showed noticeable differences over time and trials, although they viewed an
326 identical visual stimulus. This inconsistency of pupil size indirectly indicates that CGH optimization based on one's eye
327 model is hardly practical, especially when the pupil serves as a passband filter.
328

329 S3 ADDITIONAL SIMULATION RESULTS**330 Change in pupil size and its effect on holographic image quality**

331 Since the primary goal of our work is to investigate the accommodation response through holographic near-eye displays,
332 our prototype is built to have a sufficiently wide eye-box. The bandwidth is additionally halved in vertical directions
333 to match the eye-box size of holographic near-eye displays built with two different SLMs. Moreover, the eye pupil
334 functions as a finite passband preventing the holographic signal from entering the human eye. These practical issues
335 have affected the quality of reconstructed image and further influenced the experimental evaluations.
336

337 To understand the effects of band-limitation on image quality in holographic near-eye displays, we demonstrate
338 the reconstructed images when the display parameter differs, and the pupil size varies as shown in Fig. S8. The
339 reconstruction is conducted with the specification of a phase-only SLM (a resolution of 1920×1080 , a pixel pitch of
340 $6.4 \mu\text{m}$) utilized in our work. We provide the retinal images of two CGHs (8bit-SGD and 8bit-GS) reconstructed under
341 two different eyepiece lens settings (a 2-inch lens with a focal length of 40 mm and 75 mm), two band-limitation types
342 (halved and whole), and three pupil diameters (pupil diameter of 3 mm, 5 mm and 7 mm). Recall that our prototype
343 utilizes an eyepiece lens with a focal length of 75 mm, and bandwidth is vertically halved. The images demonstrated in
344 Fig. S8 imply that the holographic images are susceptible to the eye-box of the near-eye display and the changes in
345 pupil size. In addition, the image quality is relatively consistent to the change in size of eye pupil when the eye-box of
346 holographic near-eye display is sufficiently small unlike ours.
347

348 Comparison to Neural 3D holography [Choi et al., 2021]

349 Choi et al. [2021] recently introduced the adoption of alternating direction method of multipliers (ADMM) solver to
350 acquire phase-only CGHs to ensure piecewise phase smoothness of reconstructed complex-valued field. Smoothed
351 phase leads to less speckle noise in the reconstructed holographic image. The proximal gradient solvers are known to
352 effectively reduce the loss function that consists of l_2 and l_1 norm [Bach et al., 2012]. We provide the simulation results
353 of GS, SGD, and ADMM CGHs in Fig.S9. Both focused and defocused holographic images of ADMM CGHs are similar
354

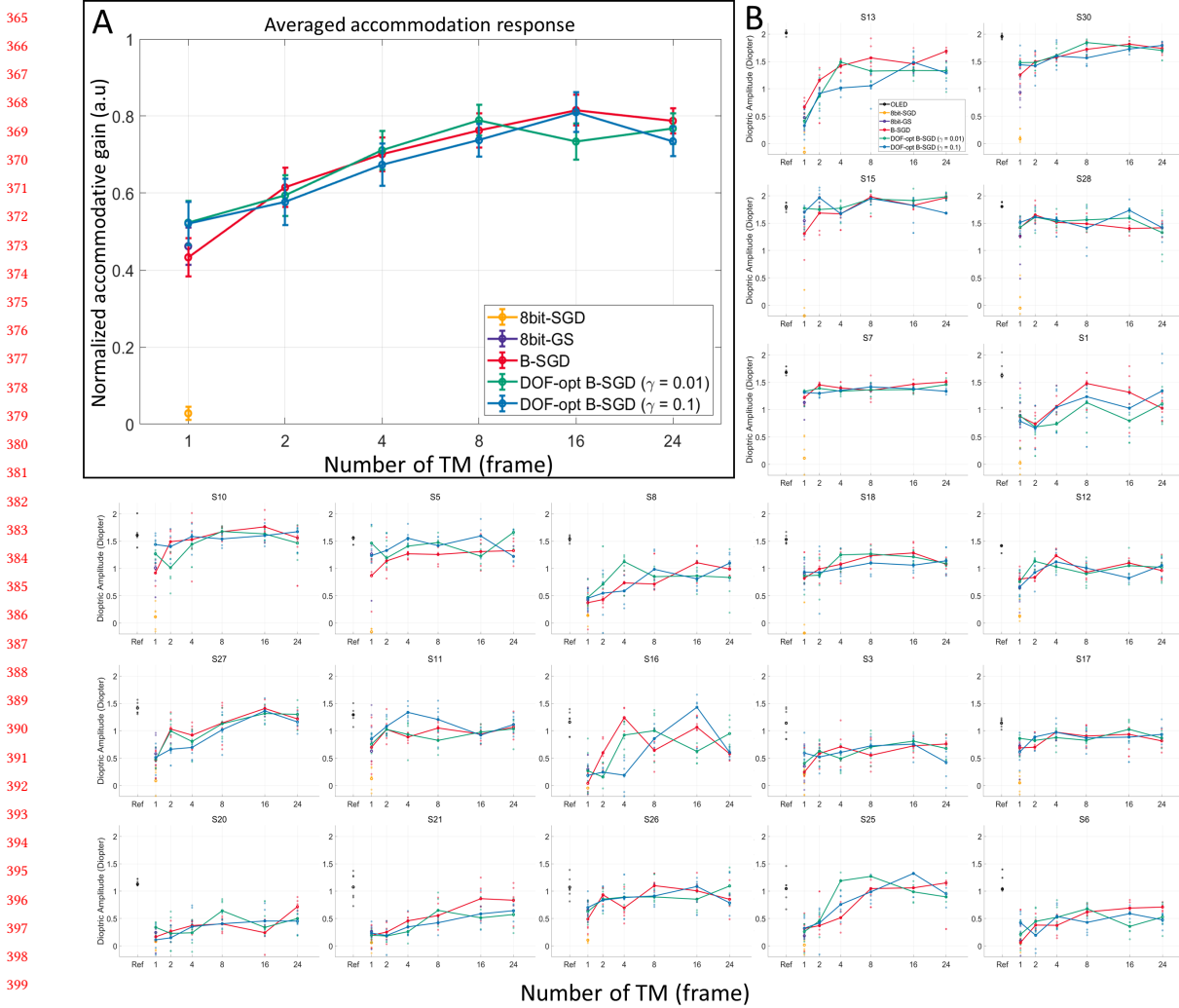


Fig. S6. Additional results of accommodation experiments. (A) Average of normalized accommodative gains measured when viewing various CGHs (8bit-SGD, 8bit-GS, B-SGD, DOF-opt B-SGD ($\gamma=0.01$), DOF-opt B-SGD ($\gamma=0.1$)). For the binary holograms (B-SGD, DOF-opt B-SGD ($\gamma=0.01, 0.1$)), holograms are realized with several TM conditions. The error bars indicate the standard error of the normalized accommodative gain measured depending on individual users. (B) Individual accommodation responses of 21 subjects are presented with the dioptric amplitudes of the fitted sinusoids. The results are sorted with the mean dioptric amplitude measured when viewing OLED (black). The dioptric amplitudes of each cycle are demonstrated with colored circles, and the excluded data are marked with additional stars.

to SGD CGHs. At the same time, the phase profile of the reconstructed field is proportionally smoothed in the case of the CGH with an ADMM solver.

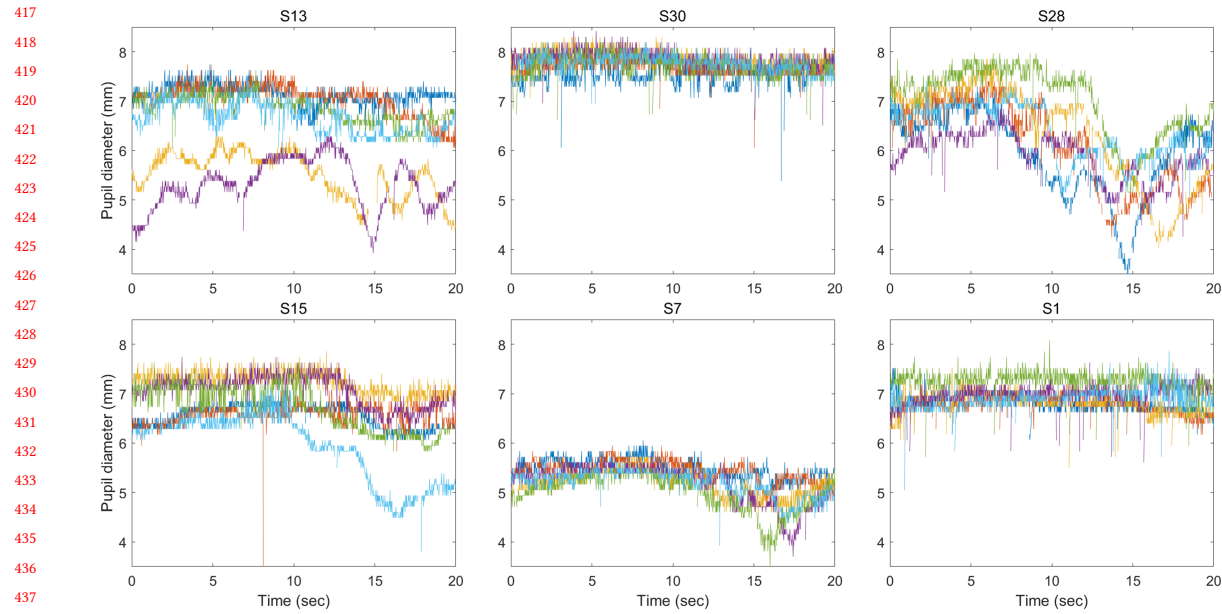


Fig. S7. Measured pupil diameter of six subjects who demonstrated highest gains with OLED viewing conditions. Each line represents a single cycle of 20 seconds.

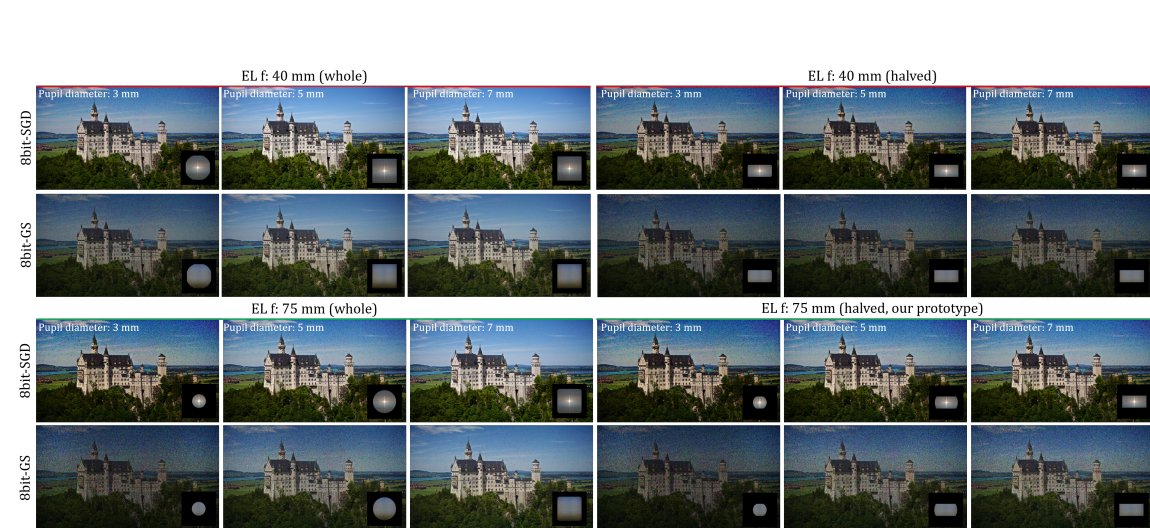


Fig. S8. Effect of band-limitation on image quality in Fresnel-type holographic near-eye displays in simulation. The retinal images of 8bit-SGD and 8bit-GS holograms were reconstructed with different eyepiece lens (EL) settings (red, green), and different pupil conditions (pupil diameter of 3 mm, 5 mm, and 7 mm) are provided. In the right bottom corner, the signal's bandwidth is demonstrated as an inset. The eye pupil acts as a finite passband limiting the holographic signals. Image sources from DIV2K dataset [Agustsson and Timofte, 2017].

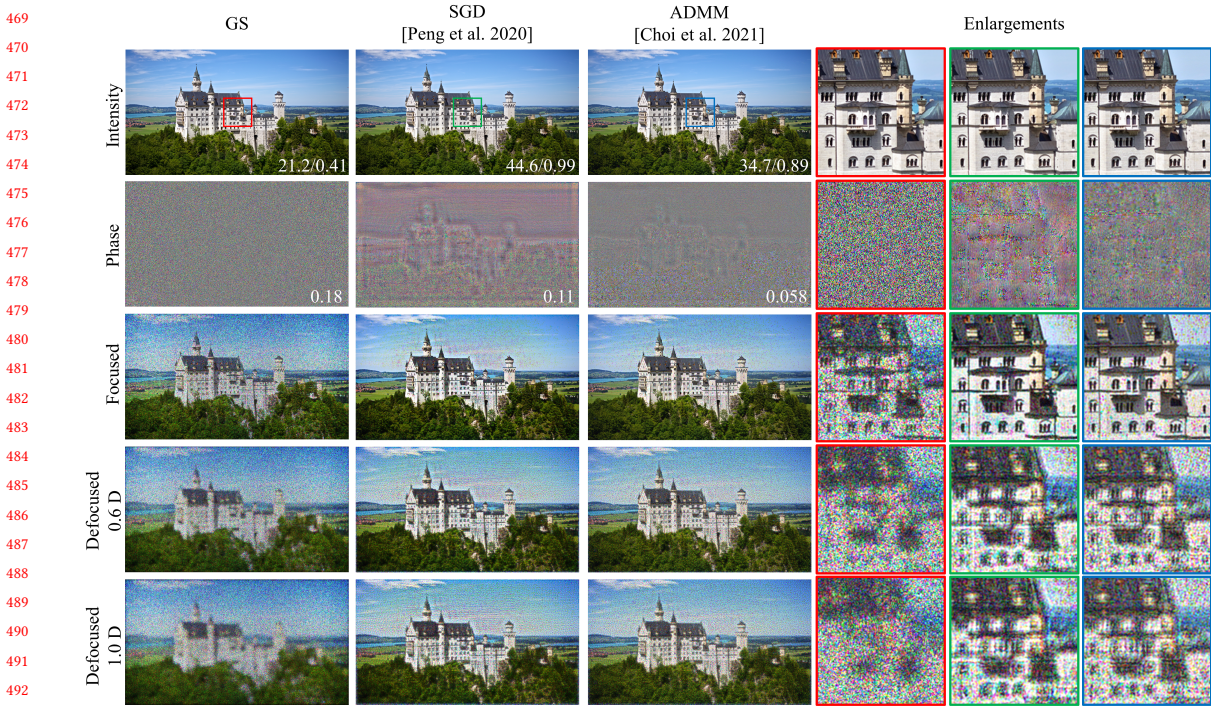


Fig. S9. Simulation results of GS, SGD, and ADMM CGHs reconstructing a single 2-D image of castle scene. We demonstrate the intensity (1st row) with additional PSNR/SSIM in the right bottom and phase profile (2nd row) with mean of magnitude of laplacian of phase at the reconstructed image plane. In addition, the intensity profiles of retinal images in the focused state (3rd row) and two different defocused states (4th row: 0.6 D and 5th row: 1.0 D) reconstructed under a pupil diameter of 3 mm are provided with additional enlargements. SGD and ADMM CGHs visualize similar focused and defocused images, while a slight difference in phase smoothness between the two images is present. Image sources from DIV2K dataset [Agustsson and Timofte, 2017].

S4 PSEUDOCODES OF CGH ACQUISITION ALGORITHMS

In this section, we provide the pseudocodes of CGH acquisition algorithms. For GS, SGD, ADMM algorithms, refer to [Choi et al., 2021, Gerchberg, 1972, Peng et al., 2020], respectively. We provide pseudocodes of Fresnel-type B-SGD [Lee et al., 2022] CGH acquisition algorithm as Algorithm 1. The binary hologram optimization procedure with contrast ratio regularization (DOF-opt B-SGD) proposed in this work is outlined as Algorithm 2.

REFERENCES

- E. Agustsson and R. Timofte. Ntire 2017 challenge on single image super-resolution: Dataset and study. In *Proceedings of the IEEE conference on computer vision and pattern recognition workshops*, pages 126–135, 2017.
- F. Bach, R. Jenatton, J. Mairal, G. Obozinski, et al. Optimization with sparsity-inducing penalties. *Foundations and Trends® in Machine Learning*, 4(1): 1–106, 2012.
- A. Bron, J. Tiffany, S. Gouveia, N. Yokoi, and L. Voon. Functional aspects of the tear film lipid layer. *Experimental eye research*, 78(3):347–360, 2004.
- P. Chakravarthula, E. Tseng, T. Srivastava, H. Fuchs, and F. Heide. Learned hardware-in-the-loop phase retrieval for holographic near-eye displays. *ACM Trans. Graph.*, 39(6), nov 2020. ISSN 0730-0301. doi: 10.1145/3414685.3417846. URL <https://doi.org/10.1145/3414685.3417846>.
- S. Choi, M. Gopakumar, Y. Peng, J. Kim, and G. Wetzstein. Neural 3D holography: Learning accurate wave propagation models for 3D holographic virtual and augmented reality displays. *ACM Trans. Graph.*, 40(6), 2021.
- R. W. Gerchberg. A practical algorithm for the determination of phase from image and diffraction plane pictures. *Optik*, 35:237–246, 1972.

Manuscript submitted to ACM

Algorithm 1 Fresnel-type B-SGD [Lee et al., 2022]

```

521: 1:  $slm$  : Pattern of binary SLM
522: 2:  $N_{iter}$  : Number of iteration
523: 3:  $J$  : Number of frames for TM
524: 4:  $\alpha$  : Learning rate
525: 5:  $g(\cdot)$  : Decoding operator for binary SLM
526: 6:  $\mathcal{P}_d(\cdot)$  : Propagation of  $d$ 
527: 7:  $\mathcal{L}_a(\cdot, \cdot)$  :  $l_2$  loss of amplitude
528: 8:  $\Gamma(\cdot)$ : sRGB gamma correction operator
529: 9: band_limit( $\cdot$ ) : Band limitation
530:
531: 10:  $a_{target} \leftarrow$  Load target amplitude with  $\sqrt{\Gamma^{-1}(I_{target})}$ 
532: 11: for  $j = 1 \dots J$  do
533: 12:    $\phi_{rand} \leftarrow$  initialize phase in a range of  $(-\pi, \pi]$ 
534: 13:    $z_0 \leftarrow \mathcal{P}_{-d}(\text{band\_limit}(a_{target} \cdot \phi_{rand}))$ 
535: 14:   for  $i = 1 \dots N_{iter}$  do
536: 15:      $a \leftarrow |\mathcal{P}_d(g(z))|$ 
537: 16:      $\{z_{i+1}, s_{i+1}\} \leftarrow \{z_i, s_i\} - \alpha \nabla \mathcal{L}_a(s_i \cdot a, a_{target})$ 
538: 17:   end for
539: 18:   return  $slm_j \leftarrow g(z)$ 
540: 19: end for
541:
```

Algorithm 2 DOF-opt B-SGD

```

542: 1:  $N$  : Number of focal states
543: 2:  $\gamma$  : Regularization coefficient
544: 3: coherent_recon( $\cdot, \Delta D$ ) : Intensity in coherent imaging / Eq.4
545: 4: incoherent_recon( $\cdot, \Delta D$ ) : Intensity in incoherent imaging / Eq.6
546: 5:  $CR_S(\cdot)$  : Contrast ratio estimated in frequency band  $S$  / Eq.5
547: 6:  $\mathcal{L}_{CR}(\cdot, \cdot)$  :  $l_1$  loss of contrast ratio
548: 7:  $a_{target} \leftarrow$  Load target amplitude with  $\sqrt{\Gamma^{-1}(I_{target})}$ 
549: 8: for  $j = 1 \dots J$  do
550: 9:    $\phi_{rand} \leftarrow$  Initialize phase in a range of  $(-\pi, \pi]$ 
551: 10:    $z_0 \leftarrow \mathcal{P}_{-d}(\text{band\_limit}(a_{target} \cdot \phi_{rand}))$ 
552: 11:   for  $i = 1 \dots N_{iter}$  do
553: 12:      $a \leftarrow |\mathcal{P}_d(g(z))|$ 
554: 13:      $u \leftarrow s \cdot \mathcal{P}_d(g(z))$ 
555: 14:      $loss_{cr} \leftarrow 0$ 
556: 15:     for  $n = 1 \dots N$  do
557: 16:        $cr_{ch} = CR_S(\Gamma(\text{coherent\_recon}(u, \Delta D_n)))$ 
558: 17:        $cr_{ih} = CR_S(\text{incoherent\_recon}(I_{target}, \Delta D_n))$ 
559: 18:        $loss_{cr} \leftarrow loss_{cr} + \frac{\gamma}{N} \mathcal{L}_{CR}(cr_{ch}, cr_{ih})$ 
560: 19:     end for
561: 20:   end for
562: 21:    $\{z_{i+1}, s_{i+1}\} \leftarrow \{z_i, s_i\} - \alpha \nabla (\mathcal{L}_a(s_i \cdot a, a_{target}) + loss_{cr})$ 
563: 22:   return  $slm_j \leftarrow g(z)$ 
564: 23: end for
565:
566:
567:
```

573 B. Lee, D. Kim, S. Lee, C. Chen, and B. Lee. High-contrast, speckle-free, true 3d holography via binary cgh optimization. *Scientific Reports*, 12(1):2811, Feb
574 2022. ISSN 2045-2322. doi: 10.1038/s41598-022-06405-2. URL <https://doi.org/10.1038/s41598-022-06405-2>.

575 Y. Peng, S. Choi, N. Padmanaban, and G. Wetzstein. Neural holography with camera-in-the-loop training. *ACM Trans. Graph.*, 39(6), nov 2020. ISSN
576 0730-0301. doi: 10.1145/3414685.3417802. URL <https://doi.org/10.1145/3414685.3417802>.

577

578

579

580

581

582

583

584

585

586

587

588

589

590

591

592

593

594

595

596

597

598

599

600

601

602

603

604

605

606

607

608

609

610

611

612

613

614

615

616

617

618

619

620

621

622

623

624